Materials Science and Engineering A 490(1-2), 343–350 (2008)

Bulk nanocrystalline $Al_{85}Ni_{10}La_5$ alloy fabricated by spark plasma sintering of atomized amorphous powders

T. T. Sasaki[a], K. Hono[b,a], J. Vierke[b] and M. Wollgarten[b], and J. Banhart[b]

[a] Graduate School of Pure and Applied Sciences, University of Tsukuba, Tsukuba 305-0047, Japan

[b] National Institute for Materials Science (NIMS), 1-2-1 Sengen, Tsukuba 305-0047, Japan

[c] Department of Materials, Hahn-Meitner-Institut Berlin, Glienicker Str. 100, D-14109 Berlin, Germany

Abstract

Amorphous $Al_{85}Ni_{10}La_5$ powders were consolidated to cylindrical samples by spark plasma sintering (SPS), and their microstructures and mechanical properties were investigated. When the powders were consolidated below the crystallization temperature, an amorphous phase was retained in the consolidated sample. Sintering above the crystallization temperature caused full crystallization. The Vickers hardness of the partially amorphous sample was about 350 HV in the as-sintered state and increased up to 450 HV by a subsequent heat treatment just below the crystallization temperature. The highest hardness was achieved in a nanocrystalline microstructure. Compression tests revealed the brittle nature of the consolidated samples although the fracture and yield strength was higher than 1 GPa. The brittleness is due to the low relative density of the partially amorphous samples and the presence of a large amount of intermetallic compounds in the fully crystallized sample.

Keywords: Al-Ni-La alloy, bulk amorphous, spark plasma sintering

1. Introduction

Interest in the study of high strength light-weight materials has increased in recent years because of the strong demands for energy saving and emission reductions in automobiles and aircrafts. Up to now, ordinary high strength Al-based alloys have been developed by the use of precipitation hardening, grain refinement, dispersion strengthening, work hardening and fiber reinforcement [1]. Generally, the upper tensile strength of wrought aluminum alloys is in the range of 550-600 MPa; the strength usually does not exceed 700 MPa. Al-RE-TM type amorphous alloys (RE: rare earth elements, TM: transition metals) were reported by two independent groups in 1988 [2,3] and opened up new possibilities for high strength aluminum alloys. The strength of the Al-RE-TM aluminum based alloy increased to 1560 MPa in amorphous/nanocrystalline composite microstructures [4]. However, the high strengths of this level were only achieved in tensile tests on small pieces of ribbon as amorphous or mixed amorphous/nanocrystalline microstructures could only be obtained by melt-spinning technique due to the lack of sufficient glass forming ability in the

Al-RE-TM systems which prevents it from being cast into moulds [5-7].

Although the crystallization behavior and the glass forming ability of Al-Ni-La amorphous alloys have been investigated by many researchers [8-11], very few studies have been carried out on the mechanical properties of the alloy system because amorphous and nanocrystalline Al-TM-RE alloys have only been available as rapidly solidified powders or ribbons. Many attempts have been made to produce bulk forms that retain a nanocrystalline/amorphous microstructure after the compaction and consolidation of gas-atomized amorphous powders and melt-spun ribbons. However, no successful results on the bulk formation of the Al-Ni-La alloy system have been reported far [12-14].

In this work, we attempted to consolidate amorphous Al-Ni-La powders by spark plasma sintering (SPS). The SPS process is considered to be one of the most promising methods for producing bulk nanocrystalline alloy with a remaining amorphous phase since its sintering temperature is much lower than those required in conventional sintering processes. The SPS process involves a rapid heating of powders by an electric current along with a simultaneous application of external pressure. Numerous experimental and theoretical investigations on the process suggest the ability of SPS to produce highly-dense powder products with the potential of nanostructure retention [15-19].

There are several reports on the consolidation of the Al-based alloys by the SPS technique [13, 14, 20-23]. Very recently, Choi et al. and Xü et al. reported that they could consolidate an amorphous Al-La-Fe-Ni powder with retaining an amorphous phase by the SPS method [13, 14]. However, the evaluation of the mechanical properties and microstructure has not been carried out extensively since the density of the alloy was not high enough for measuring the strength. In the present study, we have consolidated $Al_{85}Ni_{10}La_5$ amorphous alloy powder by SPS under various sintering conditions. The mechanical properties of the consolidated bulk samples were evaluated by compression tests and the results are discussed based on a detailed microstructural characterization to explore the possibility of producing ultra-high strength aluminum based alloys.

2. Experimental Procedure

The amorphous $Al_{85}Ni_{10}La_5$ alloy powder used in the present investigation was prepared by gas-atomization using the NANOVAL process [24]. Prior to the atomization, the alloy was synthesized in the inductively heated furnace of the atomizer under an Ar atmosphere, using pure elements Al(99.98%), Ni(99.7%) and La(99.7%). After complete melting of the pure elements, the melt was heated up to approximately 1200°C and then gas atomized using helium gas. The as-atomized powder was stored in air under ambient temperatures and humidity. The powder particle size distribution was measured using a CILAS 715 Laser Particle Analyzer. The values measured were d_{50} = 11 μm and d_{84} = 22 μm.

A secondary electron image of the atomized powder is shown in Fig. 1(a). The DSC trace and the X-ray diffraction pattern of the as-received powder in Figs. 1(b) and (c) indicate the fully amorphous nature of the as-received alloy powder. The powder showed a crystallization temperature and a glass transition temperature of 273K and 268K, respectively.

The atomized $Al_{85}Ni_{10}La_5$ powder was consolidated using a spark plasma sintering

(SPS) machine, Sumitomo Coal Mining Model Dr. Sinter-Lab. 1050. 2 g of powders were placed into a tungsten carbide die with a 10 mm diameter and sintered under vacuum at around 4.0×10^{-3} Pa for 5 to 10 min. under various sintering conditions (as listed in Table 1). Tungsten-carbide was adopted as die material so that a higher load could be applied to the powder. The consolidated alloy was water quenched right after the sintering so that further microstructure changes could be inhibited during cooling. The density of the consolidated samples was measured by the Archimedes method. Vickers hardness was measured under an applied load of 500g.

Differential scanning calorimetry (DSC) was carried out in a Perkin-Elmer Pyris-1 DSC at a heating rate of 20 K/min in the continuous heating mode or at an initial heating rate of 200 K/min for subsequent isothermal measurements. The XRD analyses were carried out with a RIGAKU RINT-2500 X-ray diffractometer using Cu-Kα radiation.

The compacts were heat-treated in an oil bath at temperatures below 473 K and in a muffle furnace for temperatures above 473 K. The mechanical properties of the sintered samples were evaluated by the compression test using cuboidal specimens of $2\times2\times4$ mm^3 at a strain rate of 1.0×10^{-4} 1/s along the long axis. The microstructural characterization of the samples was carried out using a scanning electron microscope (SEM) JEOL-5400, transmission electron microscopes (TEM), Philips CM200 operating at 200 kV and FEI Tecnai G^{2}F30 operating at 300 kV. The energy-filtered images were recorded on a CCD camera in a Tridium Gatan Imaging Filter (GIF) installed on the Tecnai G^{2}F30. Aluminum and oxygen elemental maps were recored employing the jump ratio method using the Al-K edge (1560 eV) and O-K edge (532 eV) with a 40 and 20 eV energy window width, respectively. Exposure times of 60 to 100 seconds were used to acquire each energy-filtered image. The TEM specimens were prepared by ion-milling using the Precision Ion Polishing System (GATAN 691) for the samples containing amorphous phase and electro-polishing in a solution of 33% nitric acid and 67% methanol at 233 K for fully crystallized specimens.

3. Results

3.1 Consolidation of $Al_{85}Ni_{10}La_5$ powder and mechanical properties

Based on the DSC measurements six different sintering temperatures were selected. These temperatures were chosen to be slightly below and above the crystallization temperature of T_x=456 K. Table 1 summarizes sintering temperatures, sintering times, loads, Vickers hardness and density of the sintered compacts. The relative density increases with increasing sintering temperature. The samples consolidated at temperatures higher than T_X show nearly 100 % of the theoretical density even if the applied load is decreased. The hardness value of the compact ranges from 320 to 350 HV except for the one consolidated at 473 K. Figure 1(b) also includes the DSC traces of the consolidated specimens. The DSC traces show sharp exothermic peaks, which indicate the presence of amorphous phases in the samples sintered below T_x. The first exothermic heat flow shifts to a higher temperature and its intensity decreases with increasing sintering temperature up to 523 K. These phenomena indicate an increase in the volume fraction of the crystalline phase with sintering temperature.

On the other hand, no distinct exothermic peaks were observed from the DSC trace of the sample consolidated at 753 K. This shows that the consolidation above T_x leads to a full crystallization.

Figure 1 (c) shows the XRD patterns of the samples sintered at various temperatures. With increasing sintering temperature, the crystallization of the fcc-Al phase and the intermetallic phases such as Al_3Ni and $Al_{11}La_3$ proceeds. The halo-like feature in the XRD pattern of the sample sintered below 523 K suggests that the amorphous phase remains even after sintering. In the alloy consolidated at 473 K, very small peaks corresponding to fcc-Al are confirmed in addition to the halo-like feature. The precipitation of fcc-Al becomes clear with increasing sintering temperature up to 523K. On the other hand, no halo pattern can be observed for the sample sintered at 723K, indicating full crystallization. The presence of all stable phases such as pure-Al, Al_3Ni and $Al_{11}La_3$ is confirmed.

To investigate the post-annealing effect on the hardness of the sintered sample, the samples sintered at 523 K were annealed at various temperatures for 10 min. Figure 2(a) shows the variation in the Vickers hardness as a function of annealing temperature. The highest hardness value was obtained from the alloy that was annealed at 548 K. Since this annealing temperature corresponds to the onset of the first exothermic peak in the DSC curve in Fig. 1(a), the hardening behavior is attributed to the devitrification of the amorphous phase. The effect of annealing time was also examined for specimens annealed at a temperature of 548 K. Figure 2(b) shows the variation in the Vickers hardness as a function of annealing time. The highest hardness value (450 HV) was obtained after 20 minutes of annealing, and afterwards the hardness decreased to 400 HV. Figure 2(c) shows the XRD profiles of the as-sintered specimen at 523K and the specimens annealed at 548K for 20 min and 80 min after sintering at 523K. The fully crystallized state can be revealed from the XRD profiles. Stable Al_3Ni, $Al_{11}La_3$ and fcc-Al phases are observed in these annealed specimens. Thus, crystallization is considered as being completed within the first 20 min of annealing.

Figure 3 shows the compressive nominal stress-strain curves of the samples sintered at 523 K and 753 K and subsequently annealed at 548K for 20 and 80 min. Table 2 summarizes the 0.2% off-set yield strength, fracture strength and compressive strain. All the alloys fractured without exhibiting any plastic strain. By applying the annealing treatment for 80 min, the fracture strength of the sample sintered at 523K increased up to 1341 MPa. On the other hand, the strength decreased with increasing sintering temperature from 523 K to 753 K.

3.2 Microstructure

Figure 4 shows a backscattered electron image (BEI) of the sample sintered at 523 K. The powder boundaries can be clearly observed as a dark contrast. These dark regions are considered to be pure Al. Figure 5(a) shows a TEM bright field image of the specimen containing these regions. As indicated by the arrows, the powder boundaries can be clearly seen as bright contrast. Nano-pores can also be observed as indicated in the figure. At the center of the powder particles, a different phase with a grain size of about 250 nm can be seen. These coarse grains are characterized as α-Al by the microbeam diffraction obtained from one of these grains, indicated by arrow (A), which is along the zone axis of [112] as shown in Figure 5 (b). Nanocrystalline regions are also observed as indicated by arrow (B) in

Fig. 5 (a). The selected area electron diffraction (SAED) pattern (Fig. 5(c)) taken from the nanocrystalline regions provides evidence for that these nanocrystals are fcc-Al phase embedded in the amorphous matrix. The gray regions free from diffraction contrasts are amorphous (see Fig. 5 (d)).

Figure 6(a) and (b) show the bright field and corresponding dark field TEM images from a powder boundary containing nanocrystalline particles. The dark field TEM image is taken with the {111} reflection of the fcc-Al phase. Nanocrystalline Al grains are embedded within the amorphous matrix near the powder particle boundary which shows up as bright patches. The GIF jump ratio image of oxygen in Figure 6(c) indicates a strong enrichment of oxygen along the powder boundary. The HREM image in Fig. 6(b) shows no evidence that the powder boundary of about 10 nm thickness is crystalline. Thus, the amorphous thin layer at the powder boundary is concluded to be amorphous alumina.

Figure 7 (a) and (b) show the bright field TEM image of the sample that was sintered at 523 K and subsequently annealed at 548K for (a) 20 min and (b) 80 min. Both samples are composed of nanocrystalline grains. As shown in Fig. 2 (c), nanocrystalline grains are considered to be composed of α-Al, Al_3Ni and $Al_{11}La_3$ phases. The average grain size in the sample annealed for 20 min is about 30 nm. In addition to the nano-grains, elongated particles can also be observed frequently near the particle boundary. The elongated particles were identified as fcc-Al by the EDS analysis. Grain coarsening is observed from the bright field TEM image of the alloy annealed for 80 min at 548 K as shown in Fig. 7 (b). The extended heat treatment up to 80 min resulted in a grain growth to 55 nm. The microstructure observation reveals that the coarsening of the microstructure is the main reason for the reduction in hardness from 452HV to 385HV.

Figures 8 (a) to (d) show the microstructure of the sample sintered at 753K; (a) bright field TEM image, (b) GIF jump ratio image of aluminum, (c) micro-beam diffraction pattern of the rod-like phase and (d) GIF jump ratio image of oxygen. The alloy is composed of ultra-fine grains of around 200 nm and a rod-shaped phase. Fig. 8 (b) shows that the alloy contains a substantial amount of intermetallic particles. The XRD pattern of this alloy from Fig. 2 (c) reveals that these intermetallic phases are Al_3Ni and $Al_{11}La_3$. Most of the intermetallic particles are equi-axed grains, some of them have a rod-like shape. Figure 8 (c) shows the microbeam diffraction pattern taken from one of the rod-shaped phases, which corresponds to the <101> zones of the Al_3Ni phase. Two inter-particle boundaries are marked in Fig. 8 (a), for which the presence of oxygen can be confirmed on the lower side as shown in the oxygen map in Fig. 8 (d). On the other hand, the presence of oxygen cannot be confirmed from the boundary in the upper region. The powder boundary in the bottom region has low Al concentration as indicated by the arrows in Fig. 8 (b), whereas the oxygen free-boundary does not show any concentration gradients in the Al-map.

Indications for large deformation during sintering are also found as powder particles which initially have spherical shape are transformed into elongated particles during sintering (see center of Fig. 8(a)). This large deformation is assumed to be the reason for achieving a porosity-free microstructure during sintering.

4. Discussion

The results presented in Figures 4, 5 and 6 give evidence that the crystallization occurs at the powder surface and the spherical powder shape is maintained after the consolidation below T_x. There are several reasons for the occurrence of crystallization at the powder surface. One is the increase in the local temperature ~~rise~~ at the powder surface [22, 23], and another is the decrease in the crystallization temperature by the applied pressure [26]. However, the latter is unlikely since the crystallization is only localized near the surface of the powder particles, while pressure induced crystallization is expected to occur in the whole particle volume. Since the powders are covered by an oxide layer, the temperature increases by Joule heating during the SPS process with a DC current. In some cases, a spark plasma is believed to be generated at the particle junctions. The increase in the local temperature at the powder surface would then lead there to crystallization.

Only the α-Al phase was observed as a crystallization product when the sintering temperature was below T_x as shown in Figs. 5 and 6. The crystallization occurs during the SPS process even at 473K, which is 150K lower than the crystallization temperature of this alloy as determined by the DSC measurement with the continuous heating mode at a heating rate of 20 K/min. On the other hand, the sample sintered above the crystallization temperature (753K) almost had the ideal density. The nano-voids that were observed in the sample sintered below Tx were not observed in the sample sintered above T_x.

The compressive stress-strain curves showed the brittle nature of all the alloys investigated in this work. The brittleness is attributed not only to the presence of a large amounts of the intermetallic phases but also to the presence of an oxide layers and the nano-pores due to incomplete compaction by the sintering below the crystallization temperature. A yielding behavior was observed for the alloys, which were sintered at 753K and the one annealed at 548K for 80 min after the sintering at 523K.

The fracture strength of the alloy increased from 819 MPa to 1180 MPa by the annealing treatment at 275ºC for 20 min after sintering at 250ºC. Since the major microstructural change by the heat treatment is the crystallization, the improvement of fracture strength is thought be due to this the crystallization. Although it is still unclear, the powder boundary may be strengthened by the crystallization and thus the alloy could sustain a higher load until fracture. The fracture strength can be improved further from 1180 MPa to 1341 MPa by extending the annealing time from 20 to 80 min at 548K although the hardness value decreased with annealing time. According to the compressive stress-strain curves in Figure 3, the alloy, which is annealed for 20 min. fractured within the elastic regime. On the other hand, the alloy annealed for 80 min fractured just after exhibiting the yielding behavior. In addition, the microstructure observation reveals that the grain growth from 20 nm to 50 nm occurred after annealing the sample for 80 min. In this alloy system, the plastic deformation mainly occurs at the α-Al phase grains since this phase is softer than the other intermetallic compounds such as Al_3Ni and $Al_{11}La_3$. In the α-Al phase with grain sizes below 20 ~ 30 nm, the conventional dislocation slip mechanism is reported to cease [27 - 29]. Thus, the low dislocation mobility may have reduced the fracture strength in the sample annealed for 20 min. Although the present alloy exhibited a high strength exceeding 1 GPa, which is a very high strength in the crystalline Al-based alloy, the alloy showed brittle behaviour which might stem from the large amount of intermetallic compounds and the presence of nano-

voids. (already written in the sentence before). The microstructure and the mechanical property of the alloy sintered at 753K revealed that the ductility enhancement was impossible even by the densification to the full density and by the grain coarsening. Thus, reducing the volume fraction of intermetallic phases is important for the ductility enhancement in the crystalline alloy.

5. Conclusion

$Al_{85}Ni_{10}La_5$ amorphous powders were consolidated to bulk amorphous/nanocrystalline or nanocrystalline composites by spark plasma sintering (SPS). Consolidation above the crystallization temperature led to a fully crystallized alloy with nearly full theoretical density. Subsequent heat treatment just below the onset of the crystallization peak increased the hardness from 350 HV to 450 HV. Although all specimens showed a brittle behaviour as a result of compression testing, the fracture strength of 819 MPa in the amorphous containing alloy increased up to 1340 MPa in crystalline alloy with grain size of 55 nm. The sample with grain size of 30 nm showed the highest hardness but showed lower fracture strength of 1180 MPa than the alloy with grain size of 55 nm since it fractured before yielding.

Acknowledgements

We thank Dr. G. Kumar and Dr. K. Mondal at NIMS for their valuable discussions and comments, Dr. S. Kishimoto for the SPS experiment and Dr. T. Mukai for compression test. This work was supported by the Center for Nanostructured Materials Technology (CNMT) under the 21st Century Frontier R&D Programs of the Ministry of Science and Technology, Korea through the Korea Institute of Science and Technology (KIST).

References

1. H. Jones, Aluminum Alloys, 59 (1978) 274-281.
2. Y. He, S.J. Poon, G.J. Shiflet, Science, 241 (1988) 1640-1642.
3. A. Inoue, K. Ohtera, A.P. Tsai, T. Masumoto, J. Jpn. Appl. Phys., 27 (1988) L479-L482.
4. Y.H. Kim, A. Inoue and T. Masumoto, Mater. Trans. JIM 31 (1990) 747-749.
5. A. Inoue, Prog. Mater. Sci. 43 (1998) 365-520.
6. A. Inoue and H. Kimura, Mater. Sci. and Eng. A A286 (2000) 1-10.
7. A. Inoue, S. Sobu, D.V. Louzguine, H. Kimura and K. Sasamori, J. Mater. Res. 19 (2004) 1539-1543.
8. Y.X. Zhuang, J.Z. Jiang, Z.G. Lin, M. Mezouar, W. Crichton and A. Inoue, Appl. Phys. Lett. 79 (2001) 743-745.
9. P. Si, X. Bian, W. Li, J. Zhang and Z. Yang, Phys. Lett. A 319 (2003) 424-428.
10. Z. Zhang, D. Witkin and E.J. Lavernia, J. Non-Cryst. Solids 351 (2005) 1646-1652.
11. K.L. Sahoo, M. Wollgarten, K.B. Kim and J. Banhart, J. Mater. Res. 20 (2005) 2927-2933.
12. O.N. Senkov, D.B. Miracle, J.M. Scott and S.V. Senkova, J. Alloys and Compounds 365 (2004) 126-133.
13. P.P. Choi, J.S. Kim, O.T.H. Nguyen, D.H. Kwon, Y.S. Kwon and J.C. Kim, Mater. Sci. and Eng. A 449 (2007) 1119-1122.
14. C.Y. Xu, S.S. Jia and Z.Y. Cao, J. Mater. Sci. 41 (2006) 463-466.
15. U. Anselmi-Tamburini, S. Gennari, J.E. Garay and Z.A. Munir, Mater. Sci. and Eng. A 394 (2005) 139-148.
16. U. Anselmi-Tamburini, J.E. Garay and ZA Munir, Mater. Sci. and Eng. A 407 (2005) 24-30.
17. K. Vanmeensel, A. Laptev, J. Hennicke, J. Vleugels and O. Van der Biest, Acta Mater. 53 (2005) 4379-4388.
18. E. Olevsky and L. Froyen, Scripta. Mater. 55 (2006) 1175-1178.
19. Z.A. Munir, U. Anselmi-Tamburini and M. Ohyanagi, J. Mater. Sci. 41 (2006) 763-777.
20. G. Xie, O. Ohashi, T. Yoshida, M. Song, K. Mitsuishi, H. Yasuda, K. Furuya and T. Noda, Mater. Trans. 42 (2001) 1846 – 1849.
21. E. Fleury, J.H. Lee, S.H. Kim, W.T. Kim, J.S. Kim and D.H. Kim, Metall. and Mater. Trans. 34A (2003) 841-849.
22. J. Ye, L. Ajdelstajn, J.M. Schoenung, Metall. and Mater. Trans. 37A (2006) 2059-2579.
23. A. Zuniga, L. Ajdelstajn, E.J. Lavernia, Metall. and Mater. Trans. 37A (2006) 1343-1352.
24. L. Gerking, Powder Metall. Int. 25-2 (1993) 59-65.
25. Z. Zhang, B.Q. Han, D. Witkin, L. Ajdelsztajn and E.J. Laverna, Scripta Mater. 54 (2006)

869-874.

26. F. Ye and K. Lu, Phys. Rev. B60 (1999) 7018-7024.
27. V.Y. Gertsma, M. Hoffmann, H. Gleiter and R. Birringer, Acta Metall. Mater. 42 (1994) 3539-3544.
28. R.A. Masumura, P.M. Hazzledine, C.S. Pande, Acta Mater. 46 (1998) 4527-4534.
29. V. Yamakov, D. Wolf and S.R. Phillpot, Phil.. Mag. Lett. 83(2003) 285-393.

Materials Science and Engineering A 490(1-2), 343–350 (2008)

Table

Table 1: Consolidation of the $Al_{85}Ni_{10}La_5$ alloy under various sintering conditions: parameters and results. The theoretical full density of $Al_{85}Ni_{10}La_5$ alloy is 3.53 g/cm^3 [25].

Temperature, T / K	Applied load, N / kN	Duration, T / min	Hardness, Hv	Density, ρ / g/cm^3	Relative density, %
473	35	10	203	3.23	92.2
498	35	10	323	3.36	95.8
523	35	10	341	3.43	97.6
623	12	5	346	3.44	98.1
723	12	5	352	3.50	99.9
753	12	5	338	3.50	99.9

Table 2: Summary of the mechanical property evaluation of the compacts. σ_{ys}, σ_{fs} shows the 0.2% offset yield strength and fracture stress, respectively. Annealed specimens were consolidated at 523 K.

	As-Sintered		Annealed at 548K	
	523K	753K	20min	80min
σ_{ys}, MPa	N/A	1140	N/A	1320
σ_{fs}, MPa	819	1240	1180	1341
Hardness, VHN	341	338	452	395
ε, %	N/A	0.43	N/A	0.21

Materials Science and Engineering A 490(1-2), 343–350 (2008)

Figures

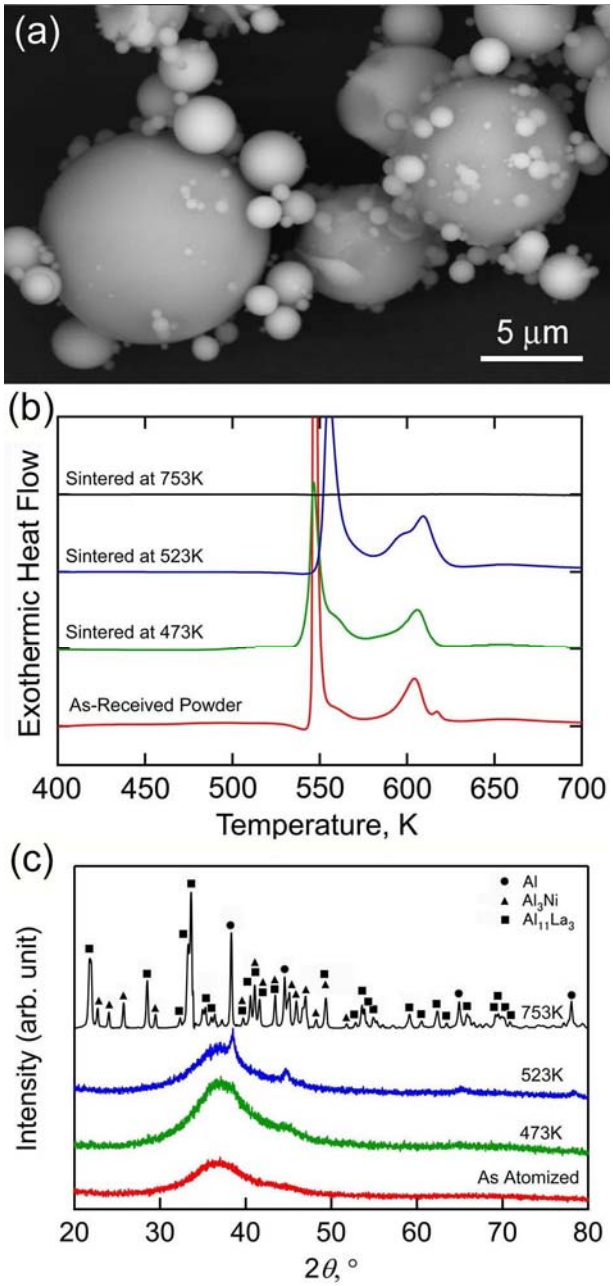

Figure 1: (a): SEM image of the as-received powder (b): DSC traces of the atomized powders and consolidated alloys at various sintering temperatures and (c): XRD patterns of the consolidated alloys at various sintering temperatures.

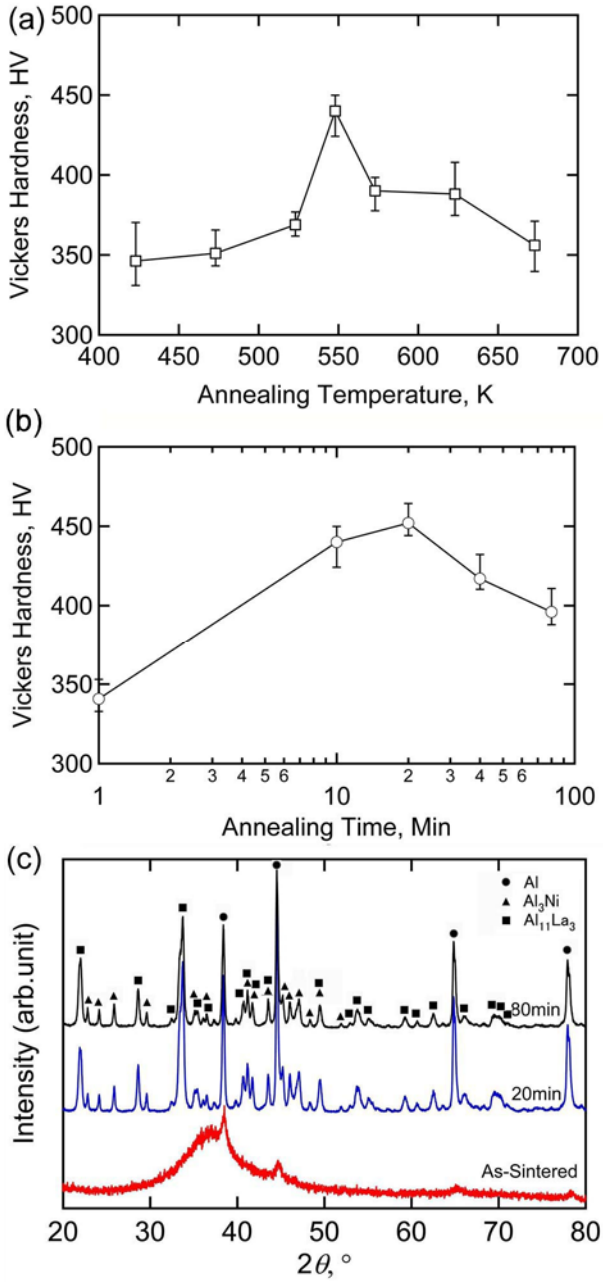

Figure 2: (a) variation of the Vickers hardness as a function of annealing temperature, (b) variation of the Vickers hardness as a function of annealing time during annealing at 548K for the alloy consolidated at 523K.

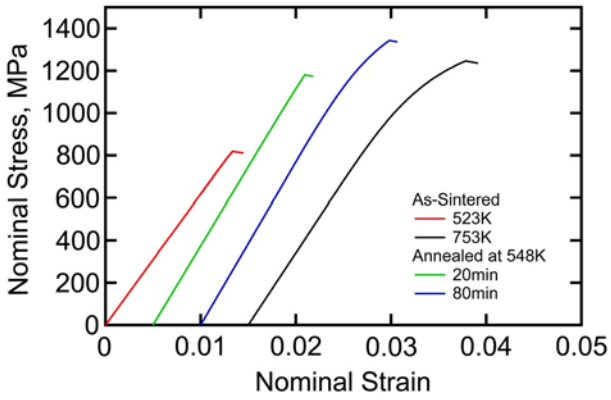

Figure 3: Nominal stress-strain curves of the consolidated alloys. Included are the stress-strain curves of the as-sintered alloy consolidated at 523 K and 753 K and of the alloy annealed for 20 and 80 minutes annealed alloy after consolidation at 523 K.

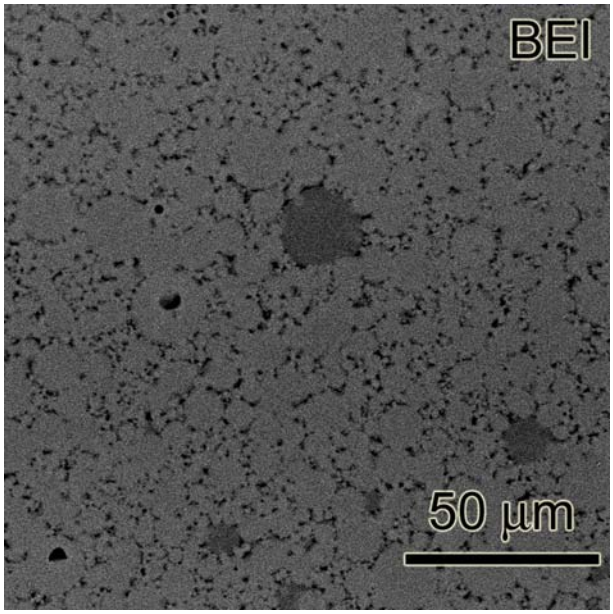

Figure 4: The back-scattered electron image (BEI) of the compacts consolidated at 523 K.

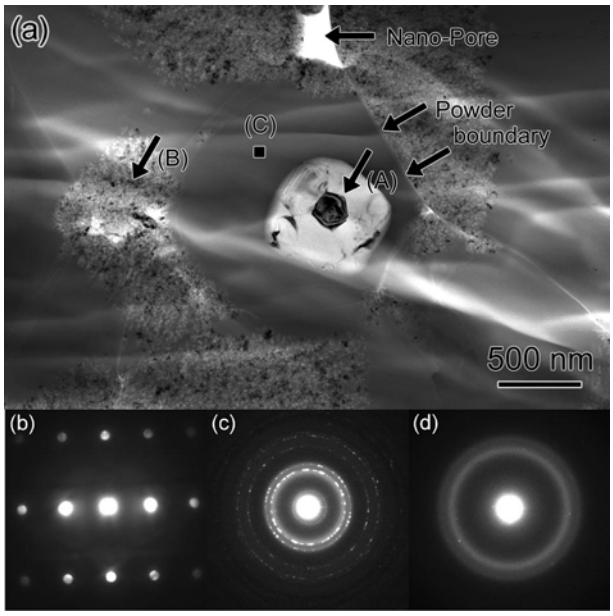

Figure 5: TEM results revealing the microstructure of the alloy consolidated at 523K. (a): bright field TEM image, (b) micro-diffraction pattern of the fcc-Al phase, (c) the SAED pattern from the primary fcc-Al nanocrystalline phase (area (B)) and (d) micro-beam diffraction pattern from the amorphous phase separated from the powder boundary (area (C)).

Materials Science and Engineering A 490(1-2), 343–350 (2008)

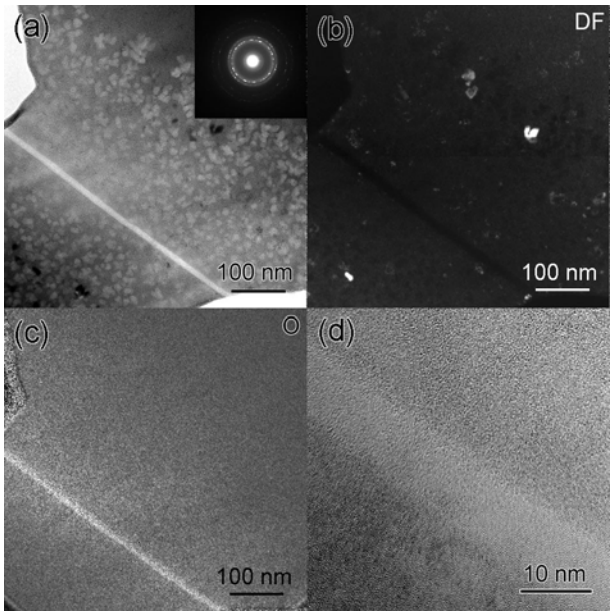

Figure 6: (a) bright field TEM image showing an inter-powder boundary surrounded by the amorphous phase containing the primary fcc-Al phase, (b) corresponding dark field TEM image, (c) oxygen map corresponding of the same area and (d) HREM images of the boundary area.

Materials Science and Engineering A 490(1-2), 343–350 (2008)

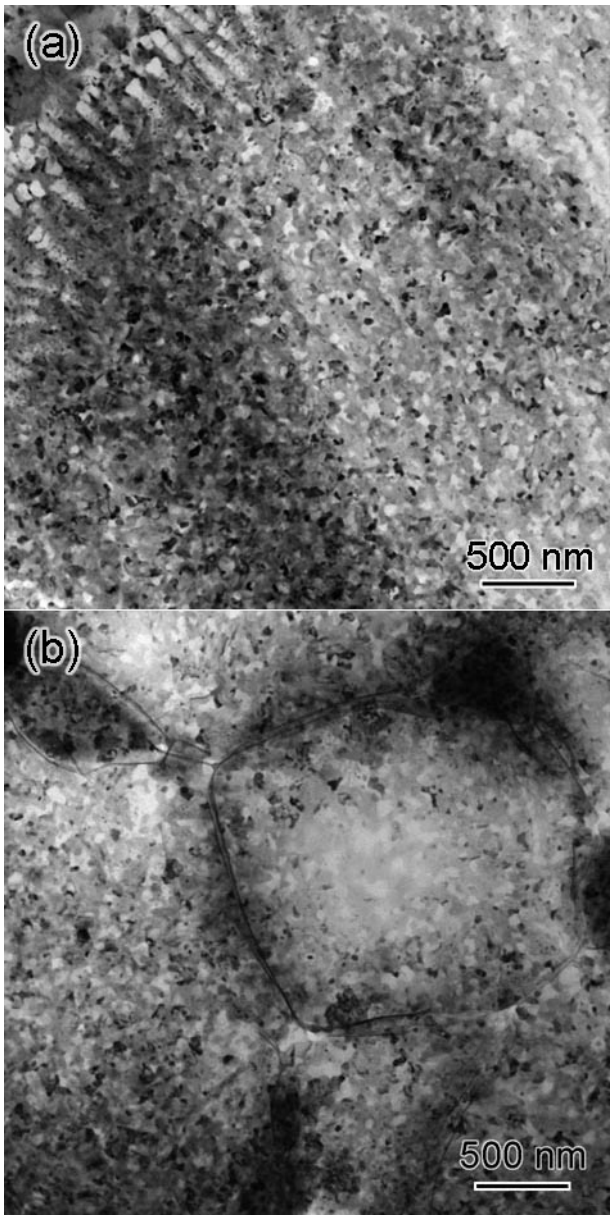

Figure 7: The bright field TEM image of the annealed alloy after sintering at 523 K, (a) annealed for 20 minutes, (b) annealed for 80 minutes.

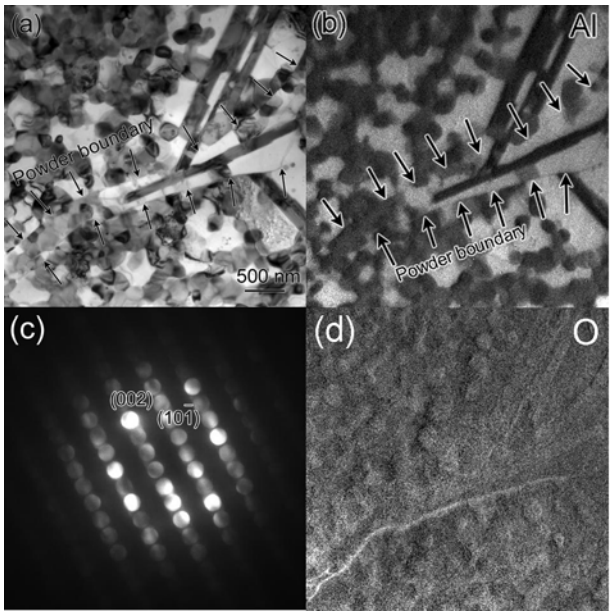

Figure 8: TEM results for the microstructure of the $Al_{85}Ni_{10}La_5$ alloy consolidated at 753 K. (a): bright field TEM bright field image, (b): Al-map, (c): micro beam diffraction pattern from one of the rod-like phases and (d): oxygen map.

Materials Science and Engineering A 490(1-2), 343–350 (2008)

Corresponding Author

T. T. Sasaki
Graduate School of Pure and Applied Sciences, University of Tsukuba,
Sengen 1-2-1, Tsukuba 305-0047, Japan (National Institute for Materials Science)
E-mail : sasaki.taisuke@nims.go.jp
Tel : +81-29-859-3354 (Ext.6727)
Fax : +81-29-859-2701